Supporting Information for

Triplet Sulfur Radical Pairs Stabilized through Hund's Rule for Ultrafast Lithium–Sulfur Batteries

Huan Li,[†] Rongwei Meng,[‡] Lars Thomsen,[§] Shuang Zhong,[†] Chao Ye,[†] Anton Tadich,[§] and Shi-Zhang Qiao[*,†]

[†]School of Chemical Engineering, Adelaide University, Adelaide, SA 5005, Australia

[‡]Department of Chemistry, National University of Singapore, 117543, Singapore

[§]Australian Synchrotron, ANSTO, 800 Blackburn Rd, Clayton, VIC 3168, Australia

*Corresponding E-mail: s.qiao@adelaide.edu.au

Experimental Section

Material Synthesis. Carbon nanotubes (CNT) were used as host material for the metal oxides. For the synthesis of Fe_3O_4 inside CNT matrix, 100 mg CNT was mixed and milling with 0.05 mmol iron phthalocyanine. Then the mixture was added to a transparent quartz crucible and placed in an 800 W microwave reactor in air. No obvious effect was observed for ≈10 s, after which there was a violent thermal reaction (flashes, the powder turned red, and a large amount of grey smoke was produced) that lasted for nearly 50 s until no smoke was produced. After cooling down, the mixture was washed to remove the large Fe_3O_4 particles and other residues. The washing steps were carried out sequentially with deionized water, 0.1 M HCl, and 0.1 M HNO_3, each under ultrasonication for 30 mins. The resulting powders were dried at 80 ^oC under vacuum for 12 h before further use. Synthesis of other metal oxide nanoparticles follows the same procedure with the same molar concentration of metals in different phthalocyanine-based metal precursors. For the synthesis of oxygen-deficient Fe_3O_{4-x}, the above-prepared Fe_3O_4 was placed in an 800 W microwave reactor in 5% H_2/Ar atmosphere for ~1 minute treatment. The etching of H_2 on Fe_3O_4 results in the production of oxygen-deficient Fe_3O_{4-x}.

Characterization Techniques. Vibrating sample magnetometry (VSM) was measured with LakeShore 7404. High-resolution STEM images were obtained under a Cs-corrected STEM (FEI Titan Cubed Themis G2 300) operated at 300 kV. Ultraviolet/visible (UV-VIS) was carried out using a spectrometer (SHIMADZU UV-2600). X-ray photoelectron spectra (XPS) were measured with the Thermo Fisher Scientific ESCALAB Xi+, Al Kα radiation. Electron paramagnetic resonance (EPR) was carried out using a Bruker ESR 5000 instrument at the measurement conditions of 2.00 mW microwave power and 9.83 GHz microwave frequency. The synchrotron-based near-edged X-ray absorption fine structure (NEXAFS) of S K-edge was performed on the soft X-ray spectroscopy beamline at Australian Synchrotron (Clayton), part of ANSTO. In-situ synchrotron XRD data were collected on the powder diffraction (PD) beamline at Australian Synchrotron. Data were collected at 30 s intervals.

Electrochemical Tests. For Li-S battery assembly and testing, the positive electrodes were prepared via mechanical mixing 80 *wt.*% S_8 (Sigma Aldrich, 99.9 %) with 20 *wt.*% substrate using a mortar, and then heated at 155 ^oC for 12 h. The substrate/S mixture was ball-milled for 12 h with aqueous acrylonitrile copolymer binder (commercial LA-133 binder) with a mass ratio of 90:10 in a sealed 3 mL plastic bottle filled with air. The ball milling was carried out in 1 mL ethanol and 1 mL deionized water (>10 MΩ cm^{-1}) using 10 of ZrO_2 balls with a diameter of 4 mm. Then the mixture was coated onto a porous carbon paper current collector (TGP-H-060, Toray) and dried at 50 ^oC under vacuum.

The carbon content among the carbon paper is 90 *wt.*%, wherein 10 *wt.*% polytetrafluoroethylene was used for surface treated to obtain a hydrophobic property. The thickness of carbon paper is 190 μm, and the porosity is 78% with a bulk density of 0.44 g cm^{-3}. Total S content in the positive electrode was 72 *wt.*%. Li-S batteries were assembled in a coin cell using a CNT coated polypropylene (PP) separator (Celgard 2400) with a diameter of 16 mm in an Ar-filled glove box (H_2O, O_2 < 0.5 ppm) by coupling the Li metal negative electrode (99%, 400 μm thick with a diameter of 14 mm) in 1 mol L^{-1} LiTfSi in DOL/DME (1:1 volume ratio) with 0.2 mol L^{-1} $LiNO_3$ as the electrolyte solution. For the preparation of CNT-coated separator, the above-mentioned CNT was ball-milled for 12 h with aqueous acrylonitrile copolymer binder (commercial LA-133 binder) with a mass ratio of 90:10 in a sealed 3 mL plastic bottle filled with air. Then, the slurry was coated onto PP separator and dried at 50 ^oC under vacuum to obtain the multilayer reduced graphene oxide coated separator. The thickness of coating layer is ≈ 10 μm. E/S mass ratio in the Li-S battery can be controlled via adding different volume of electrolyte solution. For electrochemical testing of Li-S batteries, including rate and cycling performance, the cells were galvanostatically charged and discharged at selected current rates (1C = 1.675 A g_S^{-1}) and cycles. Galvanostatic charge-discharge of all the Li-S batteries were carried out using Neware battery test system (CT-4008-5V20mA-164, Shenzhen, China). All the batteries were tested in a 25 ^oC ± 0.5 ^oC oven.

Details to Calculate the Concentration of $[S_2\cdot^- - S_2\cdot^-]$. The concentrations of $[S_2\cdot^- - S_2\cdot^-]$ radicals (**Figure 4b**) were determined using UV-vis quantification. Taking Fe_3O_4 as a representative example, sulfur was mixed with Fe_3O_4 catalyst and the sulfur (S_8) mass loading is controlled at approximately ~1 mg. The battery was then discharged to ≈ 2.02 V, which corresponds to the onset of the second discharge plateau. At this status, the high-order polysulfides (Li_2S_6 and Li_2S_8) are electrochemically reduced to Li_2S_4 and some $[S_2\cdot^- - S_2\cdot^-]$ radicals, without forming Li_2S_2 or Li_2S solids. The battery was subsequently disassembled and the electrolyte containing Li_2S_4 and $S_2\cdot^-$ was collected with DOL/DME solvent to 1000 uL mixture. Theoretically, the concentration of Li_2S_4 produced should be 7.8 mM, assuming a 100% conversion efficiency from S_8 to Li_2S_4.

In real rest, the specific capacity at this point is approximately 291 mAh g^{-1}, while the theoretical capacity is 418 mAh g^{-1}. As a result, the total concentration of Li_2S_4 and $[S_2\cdot^- - S_2\cdot^-]$ radicals produced should be calculated as $7.8 \times 291/418 = 5.44$ mM. The collected mixture was subsequently analyzed using UV-vis spectroscopy, with the results shown in **Figure 4a**. Based on the intensity at 320 nm, the Li_2S_4 concentration was determined using the standard curves (**Supplementary Figure 11**). For the Fe_3O_4 catalyst, the Li_2S_4 concentration is 1.71 mM. Therefore, the concentration of $[S_2\cdot^- - S_2\cdot^-]$ radicals is 5.44-1.71 = 3.73 mM. The ratio of $[S_2\cdot^- - S_2\cdot^-]$ radicals to Li_2S_4 is 3.73/5.44 ≈ 69%. The

same method was applied to quantify the concentration of [$S_2^{\cdot -}$ – $S_2^{\cdot -}$] radicals for other catalysts.

Model Optimization. Computations for this work were carried out using density functional theory (DFT) as implemented in VASP code. Electronic exchange-correlation energy was modeled using the Perdew-Burke-Ernzerhof (PBE) function within a generalized gradient approximation (GGA). The projector-augmented wave (PAW) method was used to describe the ionic cores. For the plane-wave expansion a 450 eV kinetic energy cut-off was used following testing a series of different cut-off energies. A Monkhorst-Pack 2×2×1 k-point grid was used to sample the Brillouin zone. Convergence criterion for the electronic structure iteration was set to 10^{-4} eV, and that for geometry optimizations was 0.02 eV $Å^{-1}$ on force. A Gaussian smearing of 0.1 eV was applied during geometry optimization and for total energy computations.

Supplementary Results

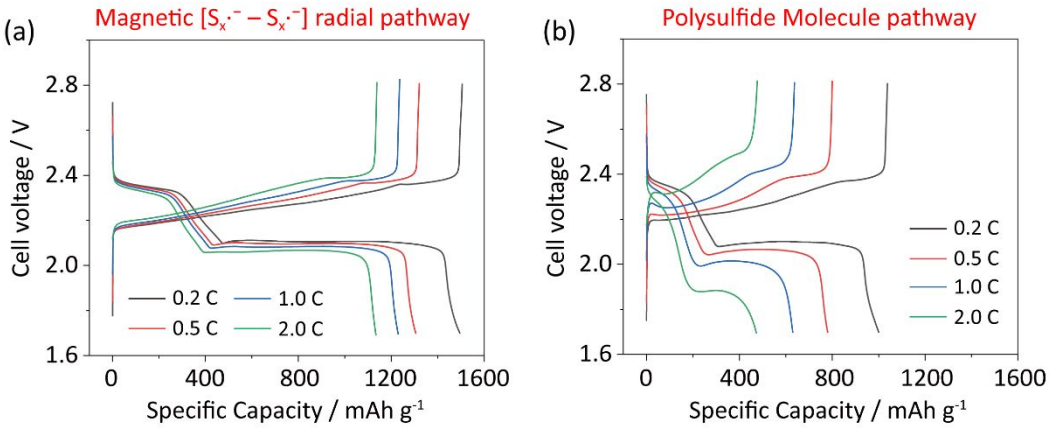

Figure S1 Galvanostatic charge-discharge curves of Li-S batteries at varying current rates (a) without catalyst and (b) with oxygen-deficient Fe_3O_{4-x} catalyst. The presence of the Fe_3O_{4-x} catalyst induces a large amount of triplet [$S_x \cdot^- - S_x \cdot^-$] radical pairs in batteries, resulting in high specific capacity at ultrafast charge-discharge rates.

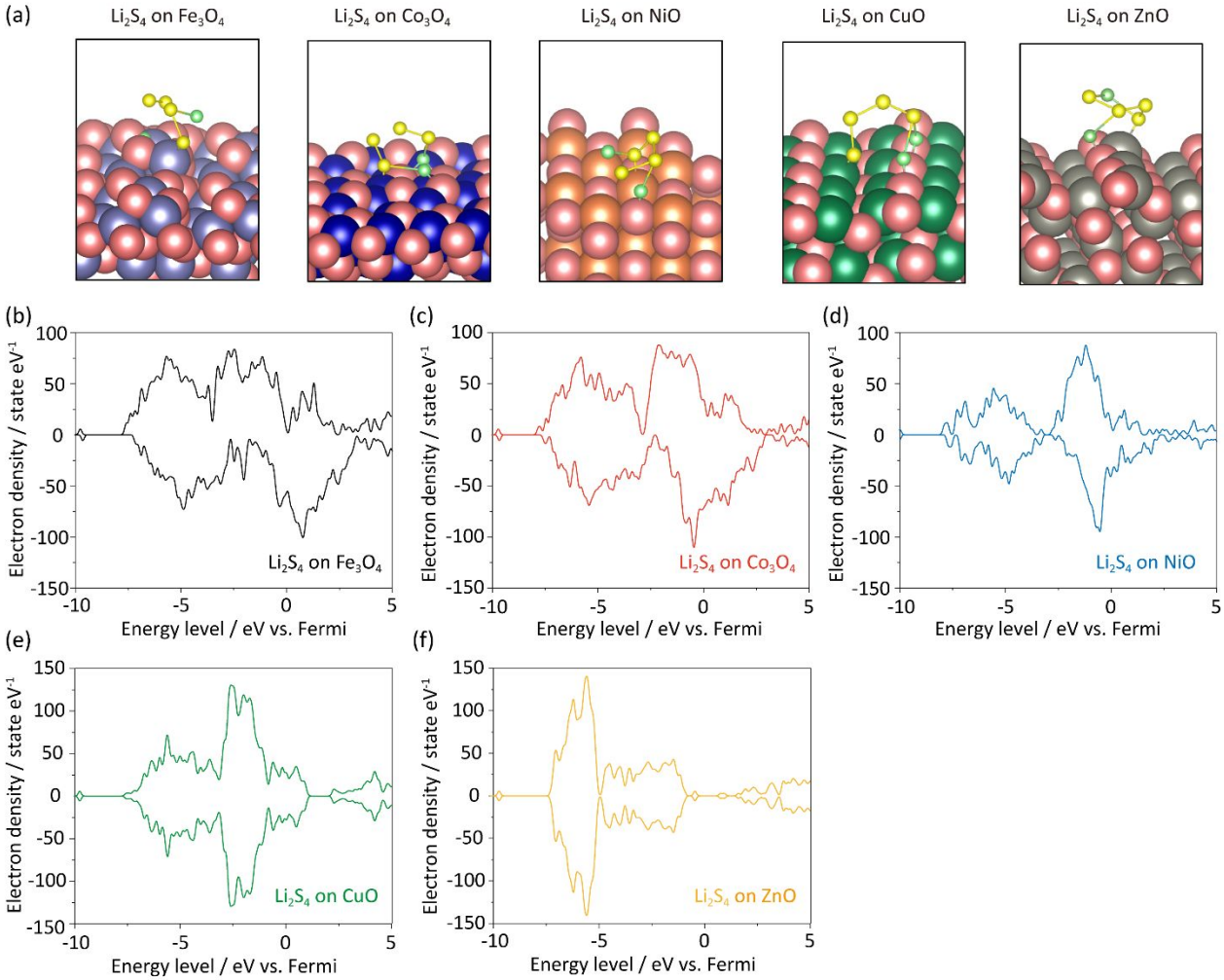

Figure S2 (a) Optimized structures of Li_2S_4 adsorbed on Fe_3O_4, Co_3O_4, NiO, CuO, and ZnO surfaces. The atoms are color-coded as follows: sulfur (yellow), lithium (green), oxygen (red), iron (brown), cobalt (dark blue), nickel (light grey), copper (light blue), and zinc (dark grey). (b-f) Corresponding total density of states (DOS) for Li_2S_4 on the surfaces of the various metal oxides: (b) Fe_3O_4, (c) Co_3O_4, (d) NiO, (e) CuO, and (f) ZnO.

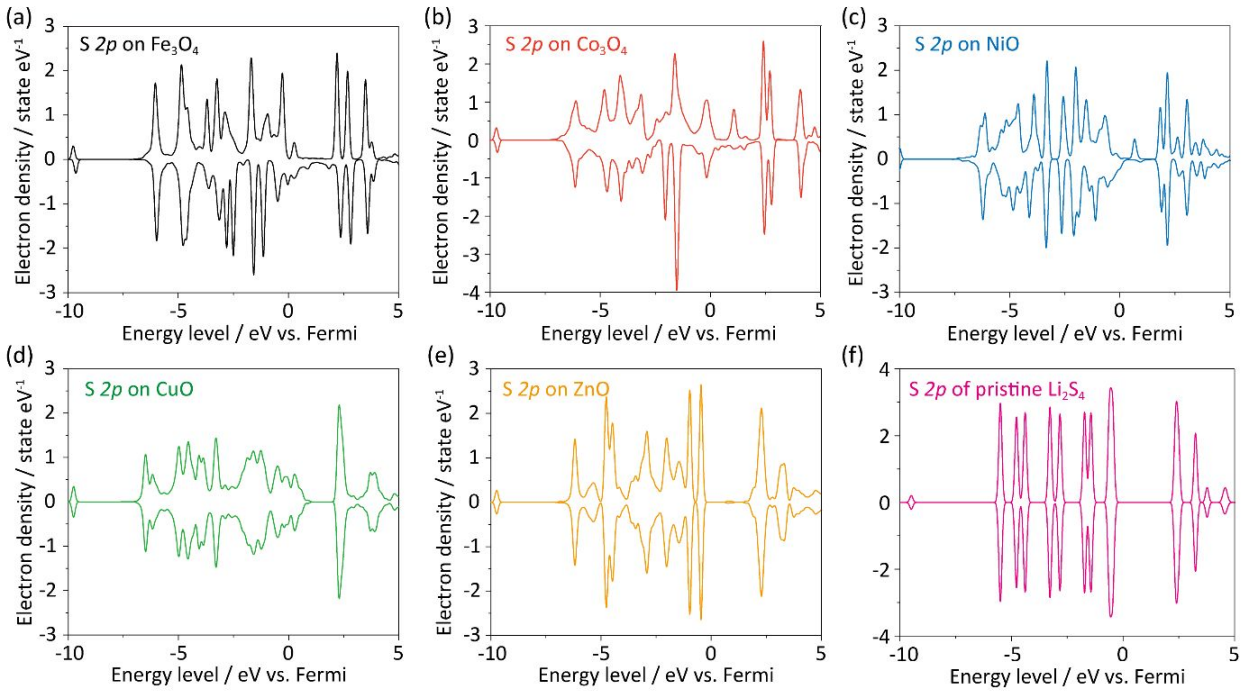

Figure S3 Projected DOS for the S 2p orbital of Li_2S_4 on the surfaces of various metal oxides (a) Fe_3O_4; (b) Co_3O_4; (c) NiO; (d) CuO; (e) ZnO and (f) pristine Li_2S_4. Curves from (a-e) are extracted from the total DOS data presented in Supplementary Figure 2.

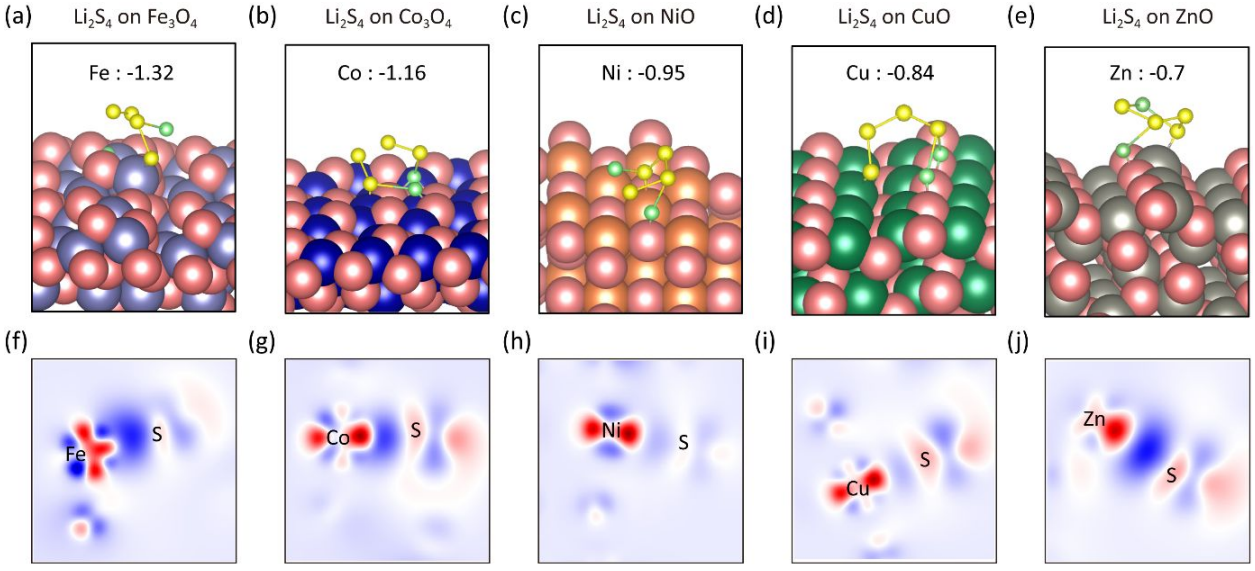

Figure S4 Bader charge analysis of the metal center for the optimized structures of Li_2S_4 on (a) Fe_3O_4; (b) Co_3O_4; (c) NiO; (d) CuO and (e) ZnO. The electron transfer from metal center to the adsorbed polysulfides follows the order: Fe_3O_4 > Co_3O_4 > NiO > CuO > ZnO. The 2D charge-transfer map illustrating electron transfer from the metal center to the sulfur atoms for (f) Fe_3O_4; (g) Co_3O_4; (h) NiO; (i) CuO and (j) ZnO. Red indicates regions of electron depletion, while blue represents electron accumulation.

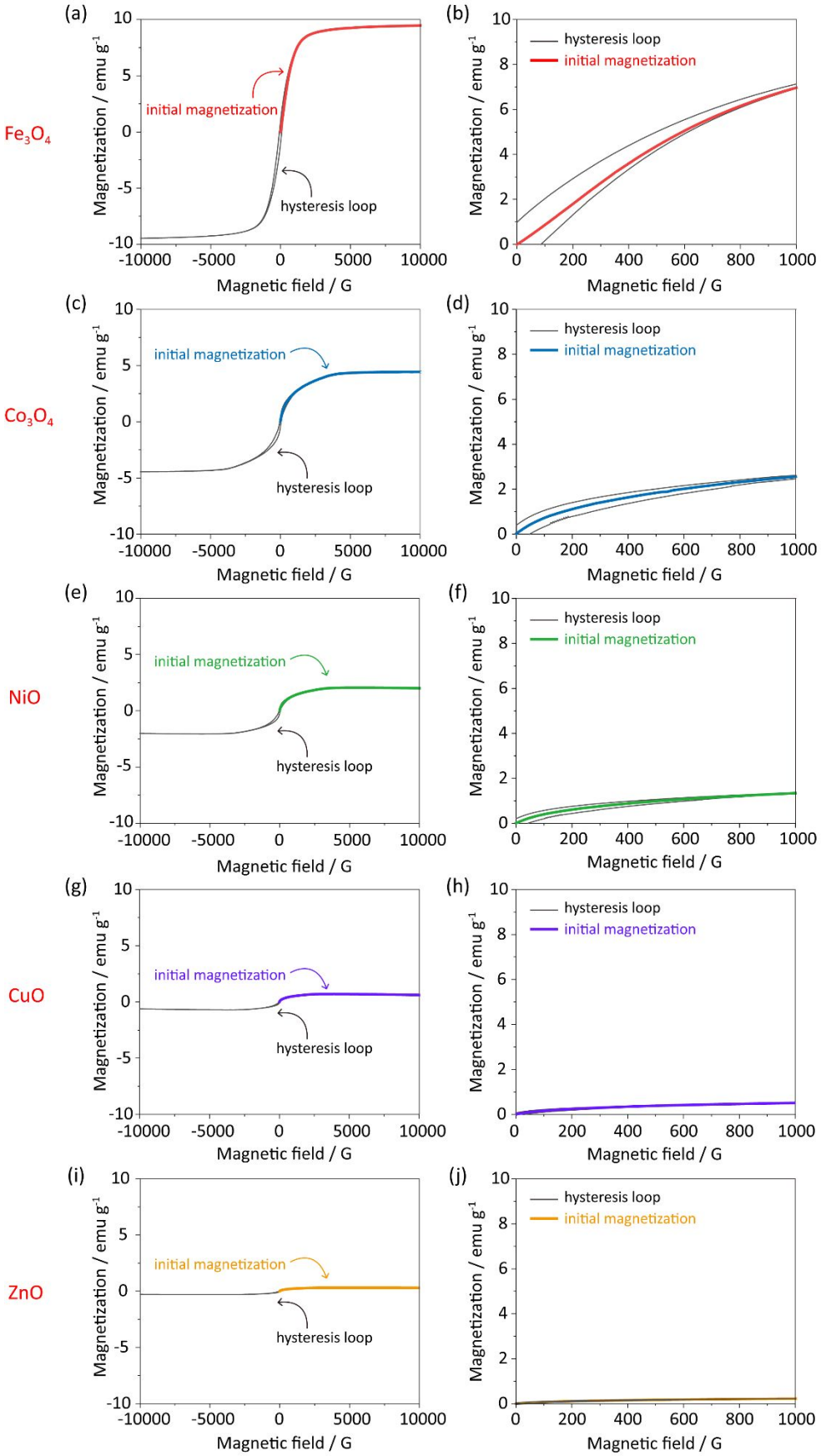

Figure S5 The hysteresis loops (M-H) and initial magnetization curves for (a, b) Fe_3O_4, (c, d) Co_3O_4, (e, f) NiO, (g, h) CuO, (i, j) ZnO on carbon nanotube substrate.

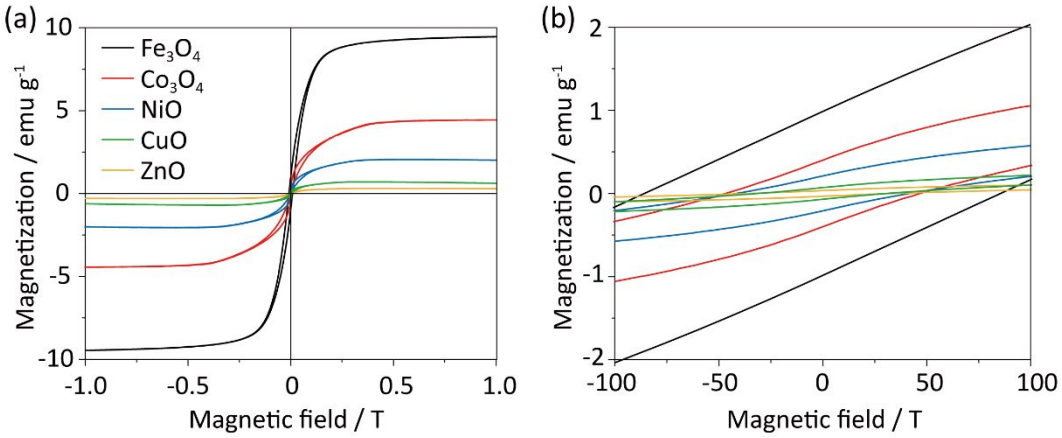

Figure S6 (a) The hysteresis loops (M-H) and (b) the values of coercivity for Fe_3O_4, Co_3O_4, NiO, CuO and ZnO. The coercivity values follow the order of Fe_3O_4 > Co_3O_4 > NiO > CuO > ZnO.

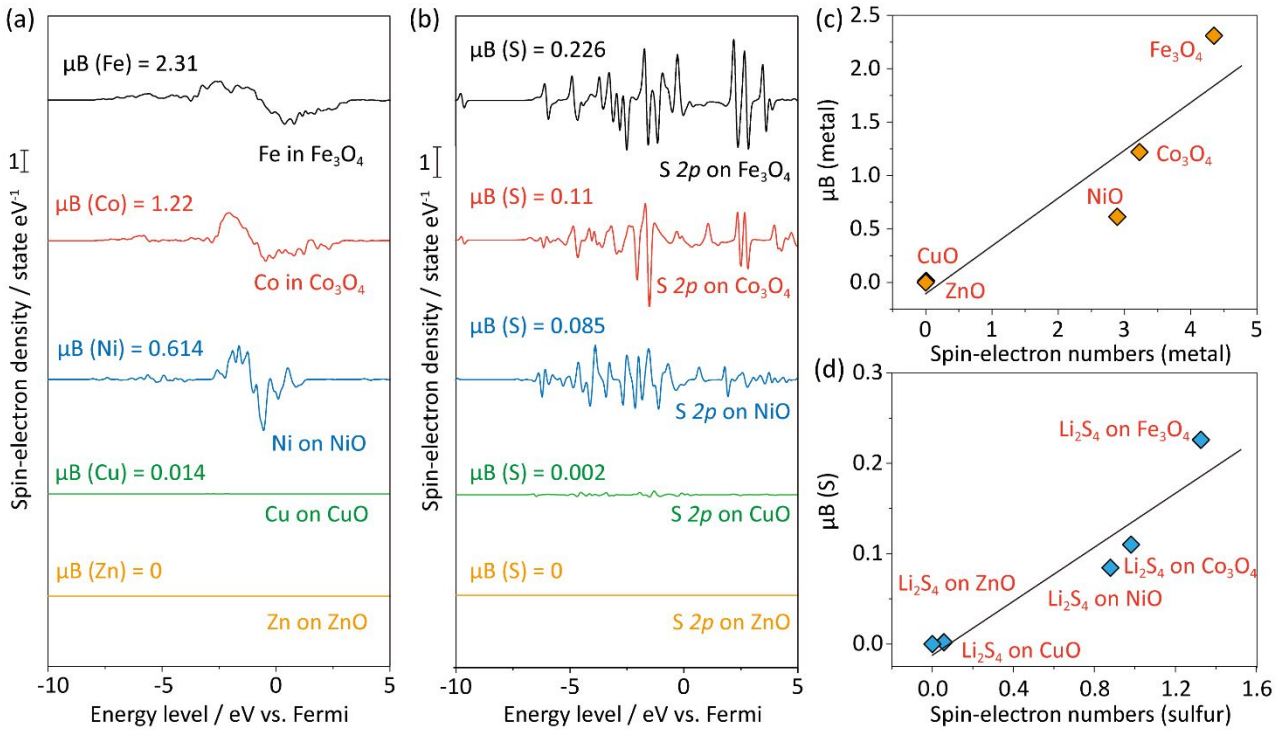

Figure S7 (a) The projected spin-electron density for each Fe, Co, Ni, Cu, Zn elements in Fe_3O_4, Co_3O_4, NiO, CuO, ZnO; (b) The projected spin-electron density for sulfur atoms in Li_2S_4 adsorbed on Fe_3O_4, Co_3O_4, NiO, CuO, ZnO; (c) Correlation between the spin-electron numbers and magnetic moments for metal elements in Fe_3O_4, Co_3O_4, NiO, CuO, ZnO; (d) Correlation between the spin-

electron numbers and magnetic moments for sulfur atoms among Li_2S_4 adsorbed on Fe_3O_4, Co_3O_4, NiO, CuO, ZnO.

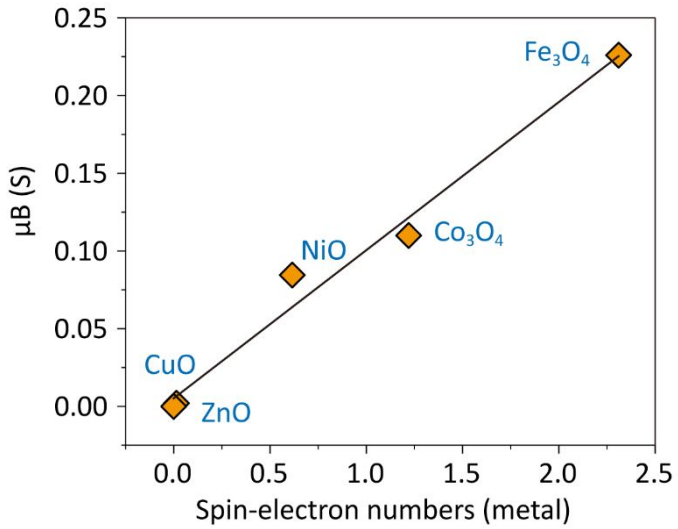

Figure S8 The relationship between spin-electron numbers of metal elements and the magnetic moments of sulfur atoms.

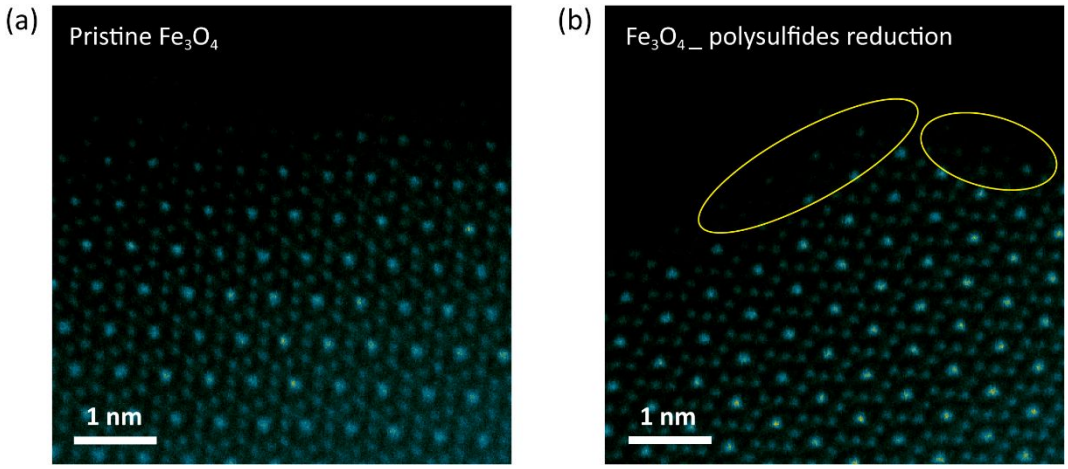

Figure S9 Aberration-corrected electron microscopy images of (a) pristine Fe_3O_4 and (b) Fe_3O_4 after polysulfide reduction. A comparison of the two images reveals significant rearrangement of surface Fe atoms following polysulfide reduction, as highlighted by the yellow circles.

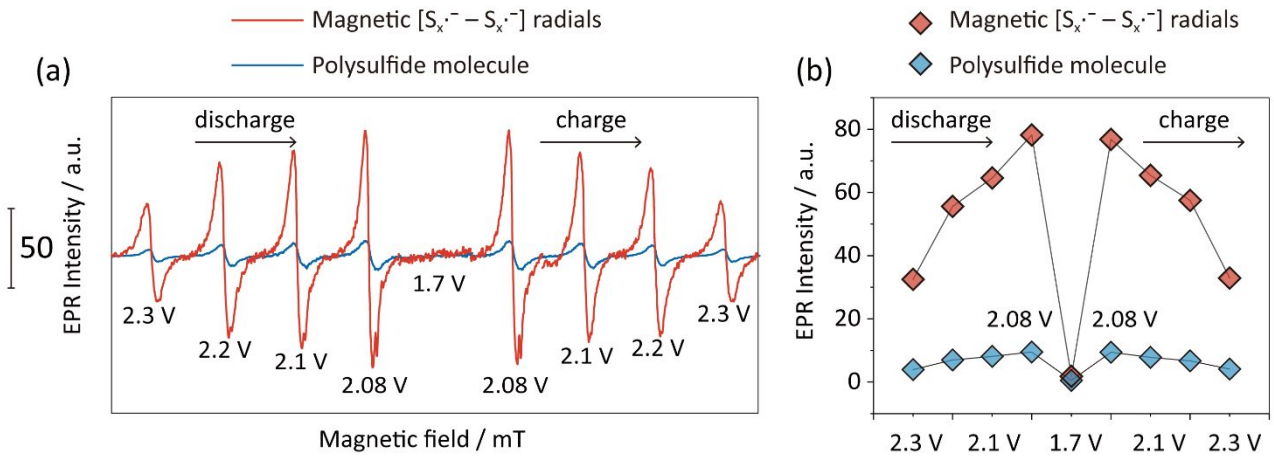

Figure S10 (a) Electron paramagnetic resonance (EPR) spectra of $[S_x\cdot^- - S_x\cdot^-]$ radicals in Li-S batteries with and without Fe_3O_4 catalyst, and (b) the corresponding EPR peak intensity at different voltages during charge-discharge. A significant increase in the concentration of $[S_4\cdot^- - S_4\cdot^-]$, $[S_3\cdot^- - S_3\cdot^-]$ and $[S_2\cdot^- - S_2\cdot^-]$ radicals is observed when using the magnetic Fe_3O_4 catalyst.

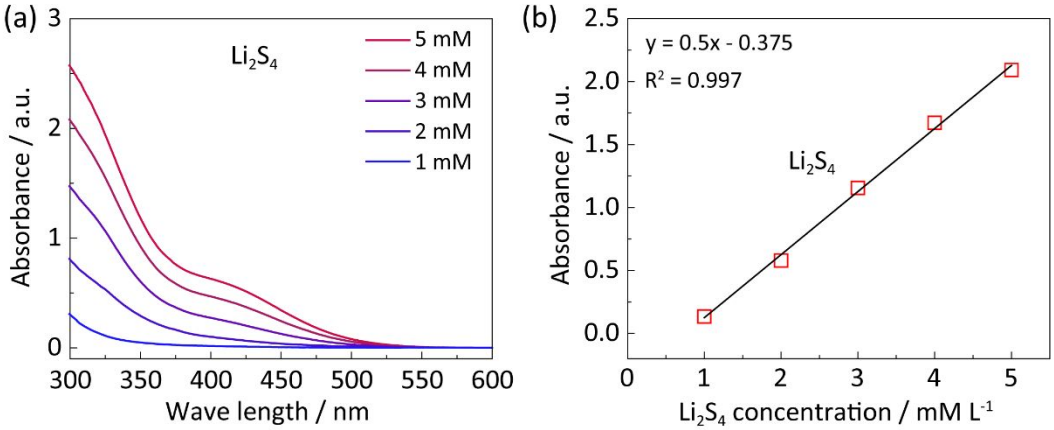

Figure S11 Standard correlation between polysulfide concentration and ultraviolet-visible (UV-vis) absorbance. (a) UV-vis spectra of Li_2S_4 solutions from 1 mM to 5 mM; (b) The linear fit between Li_2S_4 concentration and UV-vis absorbance.

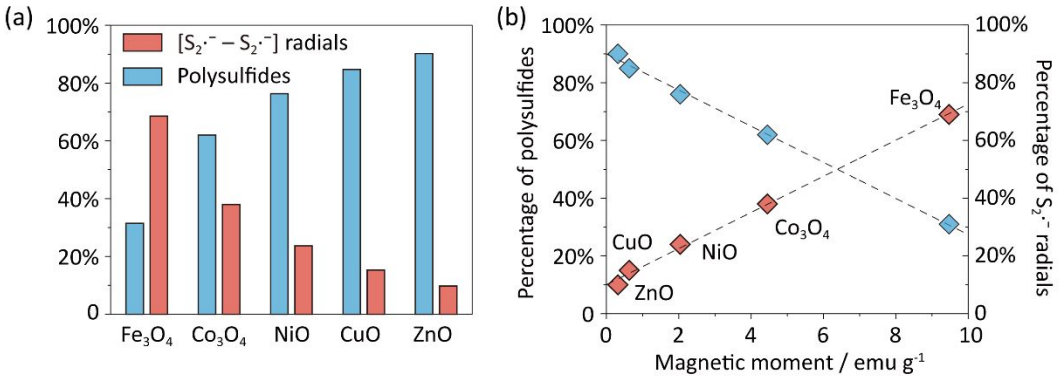

Figure S12 (a) The relative percentage of produced $[S_2^{\cdot -} – S_2^{\cdot -}]$ radicals and Li_2S_4 polysulfides in Li-S batteries with Fe_3O_4, Co_3O_4, NiO, CuO, ZnO; (b) The relationship between the magnetic moments of metal oxides and $[S_2^{\cdot -} – S_2^{\cdot -}]$ radicals with Li_2S_4 polysulfide concentrations. The magnetic moments determine the concentration of $[S_2^{\cdot -} – S_2^{\cdot -}]$ radicals. A higher magnetic moment results in more produced $[S_2^{\cdot -} – S_2^{\cdot -}]$ radicals.

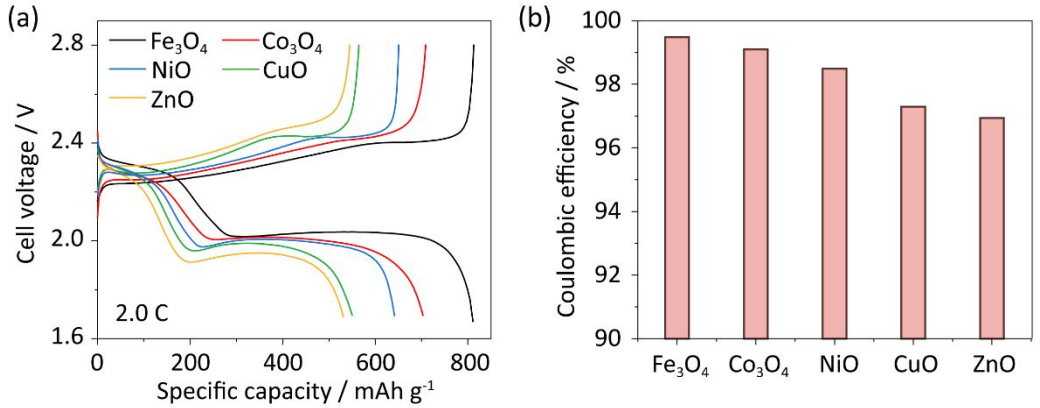

Figure S13 (a) Galvanostatic charge-discharge curves for Li-S batteries at 2.0 C with Fe_3O_4, Co_3O_4, NiO, CuO and ZnO catalysts; (b) The Coulombic efficiency for Li-S batteries with different catalysts. The Coulombic efficiency increases progressively from 96.9%, 97.3%, 98.5%, and 99.1% to 99.5% for ZnO, CuO, NiO, Co_3O_4, and Fe_3O_4, respectively. Therefore, the formation of S–S bonds during the charging process is facilitated by the presence of $[S_x^{\cdot -} – S_x^{\cdot -}]$ radical pairs.

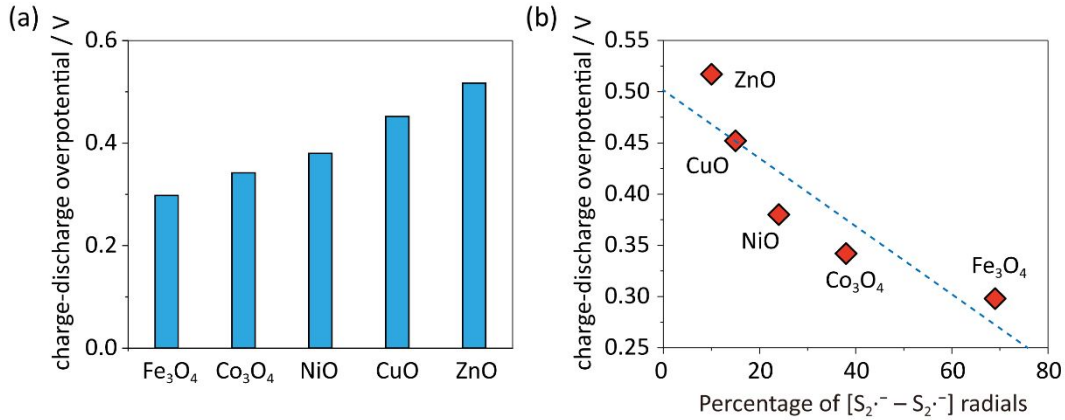

Figure S14 (a) Charge-discharge overpotentials of Li-S batteries at 2.0 C, with Fe_3O_4, Co_3O_4, NiO, CuO and ZnO catalysts; (b) The relationship between charge-discharge overpotentials and percentage of $[S_2^{\cdot -} - S_2^{\cdot -}]$ radicals.

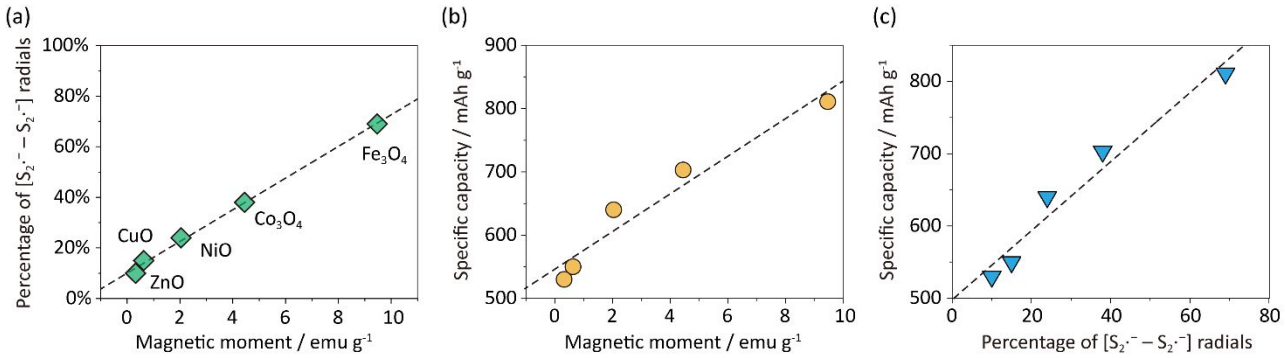

Figure S15 The relationship between magnetic moments of metal oxides, percentage of $[S_2^{\cdot -} - S_2^{\cdot -}]$ radicals and specific capacity of batteries. (a) The relationship between magnetic moments of metal oxides and percentage of $[S_2^{\cdot -} - S_2^{\cdot -}]$ radicals; (b) The relationship between magnetic moments of metal oxides and specific capacity of batteries; (c) The relationship between percentage of $[S_2^{\cdot -} - S_2^{\cdot -}]$ radicals and specific capacity of batteries.

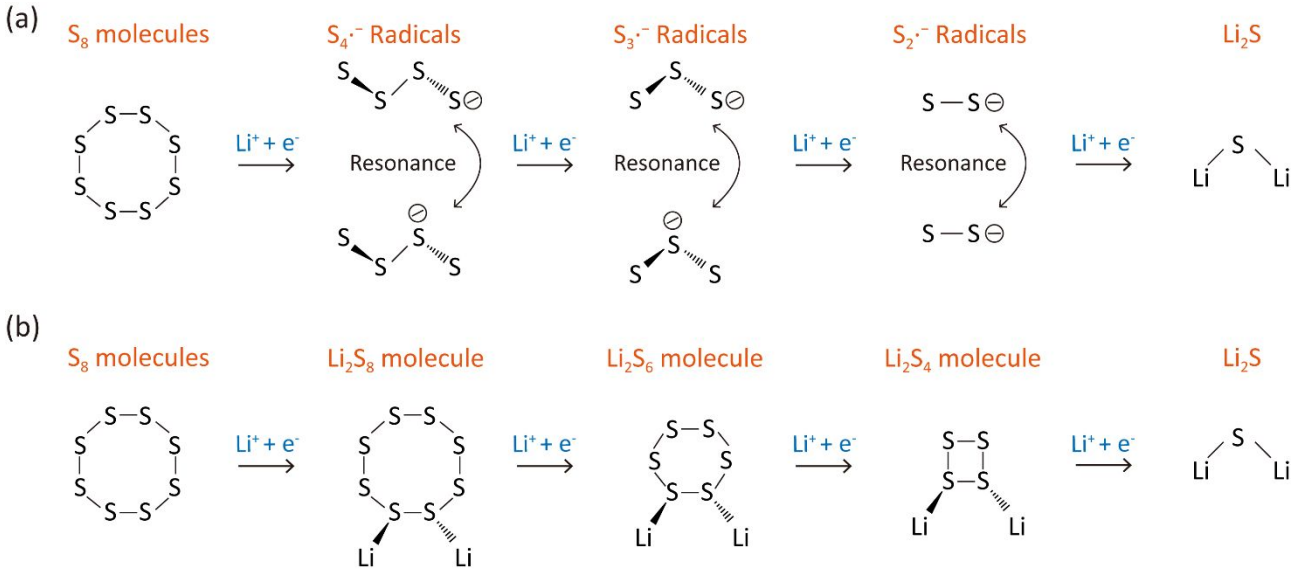

Figure S16 Sulfur conversion with (a) a magnetic free radical pathway and (b) a polysulfide molecule pathway. The magnetic free radical pathway includes the stepwise conversion of [$S_4^{\cdot -}$ – $S_4^{\cdot -}$], [$S_3^{\cdot -}$ – $S_3^{\cdot -}$] and [$S_2^{\cdot -}$ – $S_2^{\cdot -}$], with a much lower activation energy and faster conversion kinetics.

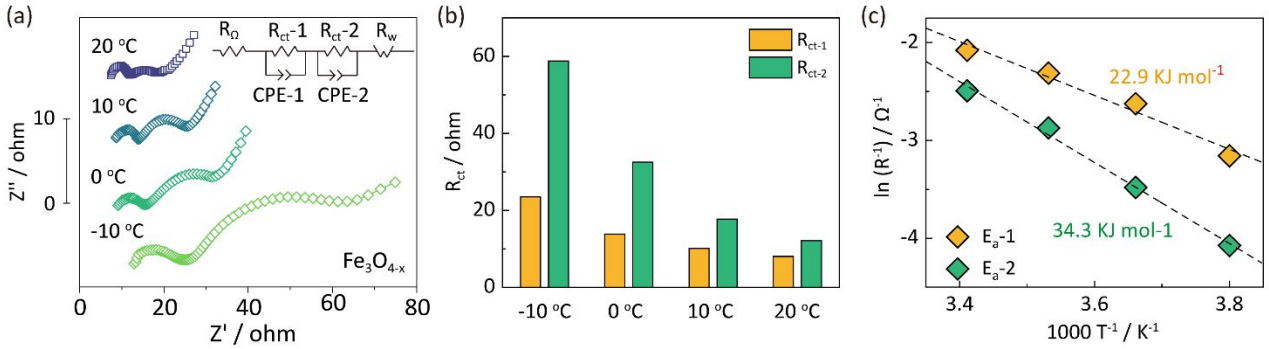

Figure S17 (a) Original and fitted electrochemical impedance spectroscopic (EIS) data for sulfur reduction in Li-S batteries with Fe_3O_{4-x} catalyst from -10 °C, 0 °C, 10 °C to 20 °C; (b) Fitted values for charge-transfer resistances (R_{ct}) for the first and second semi-circles, are denoted R_{ct-1} and R_{ct-2} respectively; (c) Corresponding Arrhenius linear-fit of value of R_{ct-1} and R_{ct-2} to determine activation energy. E_{a-1} and E_{a-2} are, respectively, for conversion from S_8 to [$S_4^{\cdot -}$ – $S_4^{\cdot -}$], [$S_3^{\cdot -}$ – $S_3^{\cdot -}$], [$S_2^{\cdot -}$ – $S_2^{\cdot -}$] radicals, and from [$S_2^{\cdot -}$ – $S_2^{\cdot -}$] radicals to Li_2S.

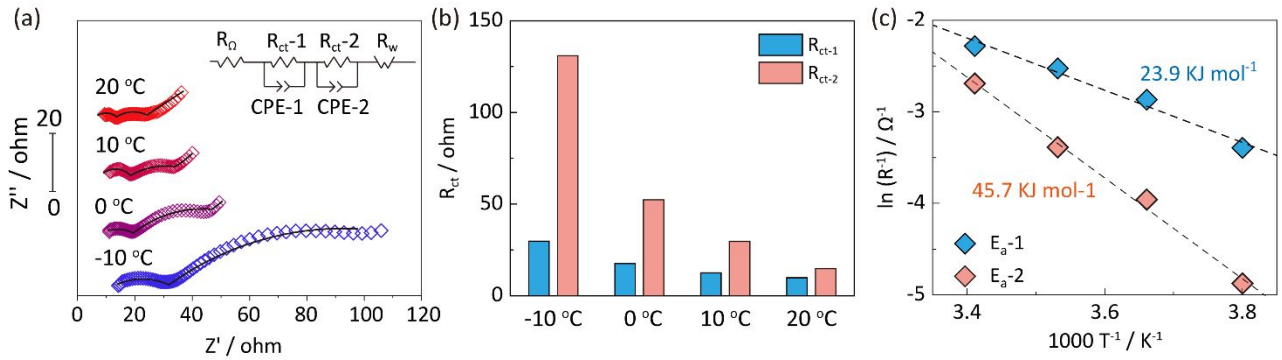

Figure S18 (a) Original and fitted electrochemical impedance spectroscopic (EIS) data for sulfur reduction in Li-S batteries with pristine carbon substrate from -10 °C, 0 °C, 10 °C to 20 °C; (b) Fitted values for charge-transfer resistances (R_{ct}) for the first and second semi-circles, are denoted R_{ct-1} and R_{ct-2} respectively; (c) Corresponding Arrhenius linear-fit of value of R_{ct-1} and R_{ct-2} to determine activation energy. E_{a-1} and E_{a-2} are, respectively, for conversion from S_8 to high-order Li_2S_4 and high-order Li_2S_4 to Li_2S.

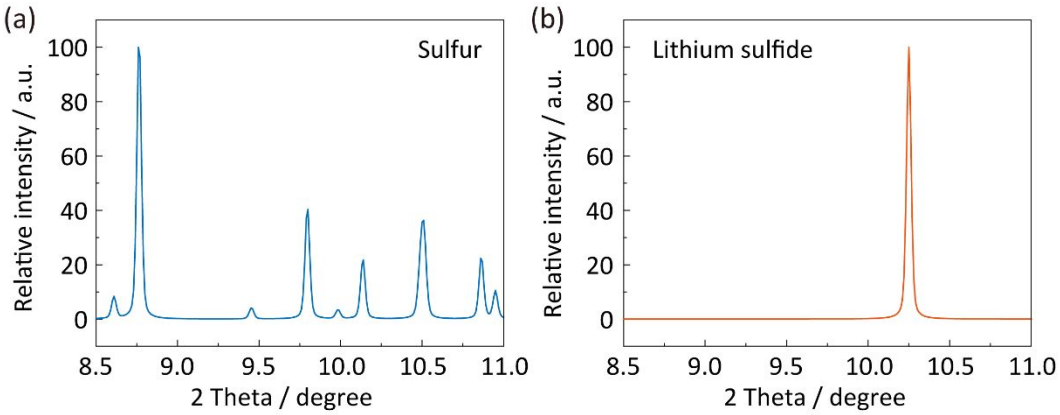

Figure S19 Simulated X-ray diffraction (XRD) patterns for (a) Sulfur and (b) Li_2S. Wavelength is 0.5903 nm. Peak positions agree well with *in-situ* synchrotron X-ray diffraction in Figures 5d and 5e.

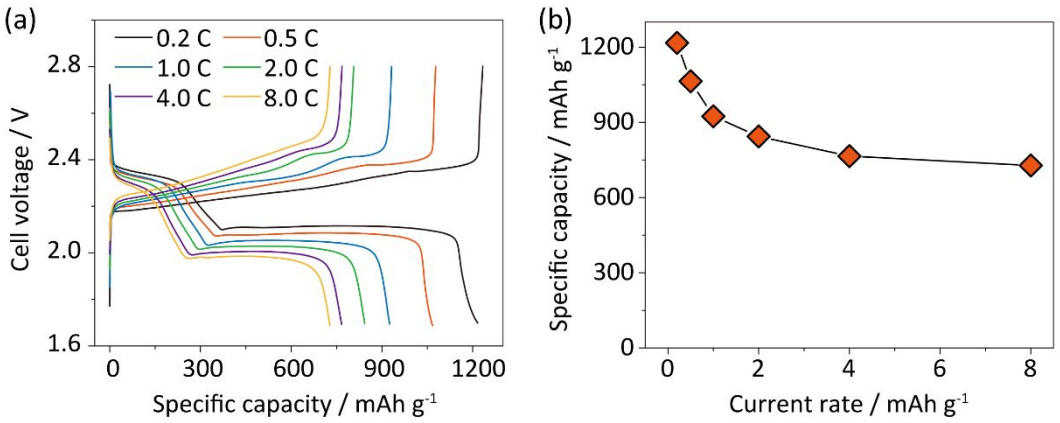

Figure S20 (a) Charge-discharge curves for Li-S batteries with Fe_3O_{4-x} catalyst from 0.2 C to 8.0 C; (b) The corresponding specific capacity at different current rates.

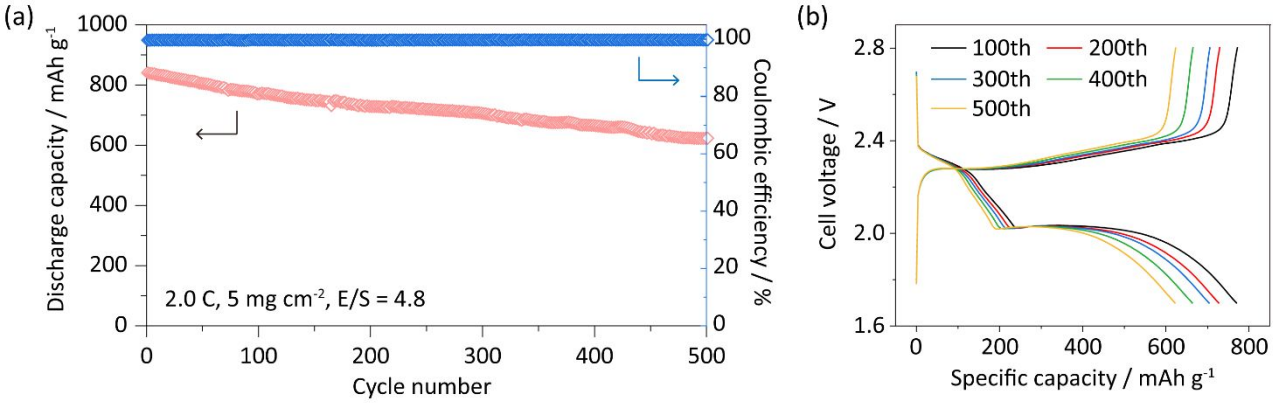

Figure S21 (a) Cycling performance of Li-S batteries with Fe_3O_{4-x} catalyst. The areal sulfur loading is 5 mg cm^{-2} and the electrolyte to sulfur mass ratio (E/S) is 4.8, with a current rate of 2.0 C. (b) The corresponding charge-discharge curves for Li-S batteries at various cycles.

Table S1 Summary comparison of performance of reported catalysts in Li-S batteries

Reported catalyst	Sulfur contents /wt. %	Testing tempera-ture / °C	Test rate /C	Specific discharge capacity /mAh g_S^{-1} (cycle number)	Areal sulfur loading /mg cm^{-2}	Electrolyte to sulfur ratio E/S	Current rate × capacity / C mAh g^{-1}	Ref
C@MoS_2	56 wt.%	RT	1.0	875	1.3	15	875	1
			2.0	730			1460	
			5.0	560			2800	
Co-NC@C	56 wt.%	25 °C	0.2	940	3.8	8.3	188	2
				805		10	161	
				725		12.5	145	
				248		16	49.6	
V_8C_7–VO_2	62 wt.%	n/a	0.2	1294	1.5	45	258.8	3
			0.5	1174			587	
			1.0	1022			1022	
			2.0	897			1794	
			4.0	768			3072	
			6.0	653			3918	
Co_4N/NG	63 wt.%	n/a	0.05	910	4.8	4.7	45.5	4
			0.1	790			79	
			0.2	300			60	
SA-Cu@NCNF	67 wt.%	n/a	0.2	844	10	10	168.8	5
				846	10	6	169.2	
ZnS-SnS@NC	64 wt.%	25 °C	0.2	1200	3.6	10	240	6
				1050	5.4	8	210	
				800	7.9	6	160	
SA-Zn-MXene	56 wt.%	n/a	0.5	905	1.7	10	452.5	7
			1.0	800			800	
			2.0	620			1240	
			6.0	515			3090	
Mo_2C/CHS	61 wt.%	n/a	0.1	1220	5	12	122	8
			0.5	1050			525	
			1.5	970			1455	
S@N-$MoSe_{2-x}$	60 wt.%	n/a	0.1	1111	3.23	~7	111.1	9
			0.2	1030			206	
			0.5	907			453.5	
			1	787			787	
In_2O_3	66 wt.%	n/a	0.12	878	9	8	105.3	10

Reported catalyst	Sulfur contents /wt. %	Testing tempera-ture / °C	Test rate /C	Specific discharge capacity /mAh g_S^{-1} (cycle number)	Areal sulfur loading /mg cm^{-2}	Electrolyte to sulfur ratio E/S	Current rate × capacity / C mAh g^{-1}	Ref
HPP	56 wt.%	n/a	0.1	988	8.1	7	98.8	11
				1410	4.4	15	141	
				1378	3.7	20	137.8	
Ni_3FeN/G	63 wt.%	n/a	0.1	950	4.8	4.7	95	12
			0.2	300			60	
$NiSe_2$	63 wt.%	n/a	0.2	850	8.8	6.0	170	13
			0.2	925	4.4	12.0	185	
Co_4W_{18}/rGO	49 wt.%	25 °C	0.05	1426	1.5	50	71.3	14
			0.1	1251			125.1	
			0.2	1171			234.2	
			0.5	1100			550	
			1	1028			1028	
			2	919			1838	
			5	644			3220	
CoZn/carbon	72 wt.%	25 °C	0.2	1071	5	4.8	214.2	15
			0.5	891			445.5	
			1.0	833			833	
			2.0	787			1574	
			4.0	740			2960	
			8.0	670			5360	
ZnS/Co-N-C	60 wt.%	RT	0.75	750	4.0	10	562.5	16
Triplet Sulfur Radical Pairs	72 wt.%	25 °C	0.2	1217	5	4.8	243.4	This work
			0.5	1064			532	
			1.0	924			924	
			2.0	844			1688	
			4.0	765			3060	
			6.0	728			5824	

References:

1. Wu, Q.; Yao, Z.; Zhou, X.; Xu, J.; Cao, F.; Li, C., Built-In Catalysis in Confined Nanoreactors for High-Loading Li-S Batteries. *ACS Nano* **2020**, 14 (3), 3365-3377.

2. Gao, H.; Ning, S.; Zhou, Y.; Men, S.; Kang, X., Polyacrylonitrile-induced formation of core-shell carbon nanocages: Enhanced redox kinetics towards polysulfides by confined catalysis in Li-S batteries. *Chem. Eng. J.* **2021**, 408, 127323.

3. Cai, J.; Jin, J.; Fan, Z.; Li, C.; Shi, Z.; Sun, J.; Liu, Z., 3D Printing of a V_8C_7-VO_2 Bifunctional Scaffold as an Effective Polysulfide Immobilizer and Lithium Stabilizer for Li-S Batteries. *Adv. Mater.* **2020**, 32 (50), e2005967.

4. Zhao, M.; Peng, H. J.; Li, B. Q.; Chen, X.; Xie, J.; Liu, X.; Zhang, Q.; Huang, J. Q., Electrochemical Phase Evolution of Metal-Based Pre-Catalysts for High-Rate Polysulfide Conversion. *Angew. Chem. Int. Ed.* **2020**, 59 (23), 9011-9017.

5. Xiao, R.; Yu, T.; Yang, S.; Chen, K.; Li, Z.; Liu, Z.; Hu, T.; Hu, G.; Li, J.; Cheng, H.-M.; Sun, Z.; Li, F., Electronic structure adjustment of lithium sulfide by a single-atom copper catalyst toward high-rate lithium-sulfur batteries. *Energy Storage Mater.* **2022**, 51, 890-899.

6. Yao, W.; Zheng, W.; Xu, J.; Tian, C.; Han, K.; Sun, W.; Xiao, S., ZnS-SnS@NC Heterostructure as Robust Lithiophilicity and Sulfiphilicity Mediator toward High-Rate and Long-Life Lithium-Sulfur Batteries. *ACS Nano* **2021**, 15 (4), 7114-7130.

7. Zhang, D.; Wang, S.; Hu, R.; Gu, J.; Cui, Y.; Li, B.; Chen, W.; Liu, C.; Shang, J.; Yang, S., Catalytic Conversion of Polysulfides on Single Atom Zinc Implanted MXene toward High-Rate Lithium-Sulfur Batteries. *Adv. Funct. Mater.* **2020**, 30 (30), 2002471.

8. Qian, J.; Xing, Y.; Yang, Y.; Li, Y.; Yu, K.; Li, W.; Zhao, T.; Ye, Y.; Li, L.; Wu, F.; Chen, R., Enhanced Electrochemical Kinetics with Highly Dispersed Conductive and Electrocatalytic Mediators for Lithium-Sulfur Batteries. *Adv. Mater.* **2021**, 33 (25), e2100810.

9. Shi, Z.; Sun, Z.; Cai, J.; Yang, X.; Wei, C.; Wang, M.; Ding, Y.; Sun, J., Manipulating Electrocatalytic Li_2S Redox via Selective Dual-Defect Engineering for Li-S Batteries. *Adv. Mater.* **2021**, 33 (43), e2103050.

10. Hua, W.; Li, H.; Pei, C.; Xia, J.; Sun, Y.; Zhang, C.; Lv, W.; Tao, Y.; Jiao, Y.; Zhang, B.; Qiao, S. Z.; Wan, Y.; Yang, Q. H., Selective Catalysis Remedies Polysulfide Shuttling in Lithium‐Sulfur Batteries. *Adv. Mater.* **2021**, 33 (38), 2101006.

11. Ye, Z.; Jiang, Y.; Li, L.; Wu, F.; Chen, R., A High-Efficiency CoSe Electrocatalyst with Hierarchical Porous Polyhedron Nanoarchitecture for Accelerating Polysulfides Conversion in Li-S Batteries. *Adv. Mater.* **2020**, 32 (32), 2002168.

12. Zhao, M.; Peng, H.-J.; Zhang, Z.-W.; Li, B.-Q.; Chen, X.; Xie, J.; Chen, X.; Wei, J.-Y.; Zhang, Q.; Huang, J.-Q., Activating Inert Metallic Compounds for High-Rate Lithium -Sulfur Batteries Through In Situ Etching of Extrinsic Metal. *Angew. Chem. Int. Ed.* **2019**, 58 (12), 3779-3783.

13. Shao, A. H.; Zhang, X.-X.; Zhang, Q.-S.; Li, X.; Wu, Y.; Zhang, Z.; Yu, J.; Yang, Z.-Y., Ultrathin Nanosheet-Assembled Flowerlike $NiSe_2$ Catalyst Boosts Sulfur Redox Reaction Kinetics for Li–S Batteries. *ACS Applied Energy Mater.* **2021**, 4 (4), 3431-3438.

14. Lei, J.; Fan, X. X.; Liu, T.; Xu, P.; Hou, Q.; Li, K.; Yuan, R. M.; Zheng, M. S.; Dong, Q. F.; Chen, J. J., Single-dispersed polyoxometalate clusters embedded on multilayer graphene as a bifunctional electrocatalyst for efficient Li-S batteries. *Nat. Commun.* **2022**, 13 (1), 202.

15. Li, H.; Meng, R.; Ye, C.; Tadich, A.; Hua, W.; Gu, Q.; Johannessen, B.; Chen, X.; Davey, K.; Qiao, S. Z., Developing high-power Li||S batteries via transition metal/carbon nanocomposite electrocatalyst engineering. *Nat. Nanotechnol.* **2024**, 19, 792-799.

16. Zhao, C.; Xu, G.-L.; Yu, Z.; Zhang, L.; Hwang, I.; Mo, Y.-X.; Ren, Y.; Cheng, L.; Sun, C.-J.; Ren, Y.; Zuo, X.; Li, J.-T.; Sun, S.-G.; Amine, K.; Zhao, T., A high-energy and long-cycling lithium–sulfur pouch cell via a macroporous catalytic cathode with double-end binding sites. *Nat. Nanotechnol.* **2020**, 16, 166-173.